

Second-order cone interior-point method for quasistatic and moderate dynamic cohesive fracture*

Stephen A. Vavasis[†] Katerina D. Papoulia[‡] M. Reza Hirmand[§]

September 25, 2019

Abstract

Cohesive fracture is among the few techniques able to model complex fracture nucleation and propagation with a sharp (nonsmeared) representation of the crack. Implicit time-stepping schemes are often favored in mechanics due to their ability to take larger time steps in quasistatic and moderate dynamic problems. Furthermore, initially rigid cohesive models are typically preferred when the location of the crack is not known in advance, since initially elastic models artificially lower the material stiffness. It is challenging to include an initially rigid cohesive model in an implicit scheme because the initiation of fracture corresponds to a nondifferentiability of the underlying potential. In this work, an interior-point method is proposed for implicit time stepping of initially rigid cohesive fracture. It uses techniques developed for convex second-order cone programming for the nonconvex problem at hand. The underlying cohesive model is taken from Papoulia (2017) and is based on a nondifferentiable energy function. That previous work proposed an algorithm based on successive smooth approximations to the nondifferential objective for solving the resulting optimization problem. It is argued herein that cone programming can capture the nondifferentiability without smoothing, and the resulting cone formulation is amenable to interior-point algorithms. A further benefit of the formulation is that other conic inequality constraints are straightforward to incorporate. Computational results are provided showing that certain contact constraints can be easily handled and that the method is practical.

1 A nondifferentiable energy model for cohesive fracture

In this section, we review prior work by Papoulia [21] as well as related works on nondifferentiable energy models for fracture. We assume isothermal conditions throughout so that temperature effects can be neglected and consideration of thermodynamics reduces to mechanical potential and kinetic energy.

Let $\Omega \subset \mathbf{R}^{n_{\text{dim}}}$ ($n_{\text{dim}} = 2, 3$) denote the initial configuration of the body under consideration. Let $\mathcal{S} \subset \Omega$ be a union of $(n_{\text{dim}} - 1)$ -dimensional surfaces (when $n_{\text{dim}} = 3$) or curves (when $n_{\text{dim}} = 2$) that may each cut across the entire domain. Let $u : \Omega \rightarrow \mathbf{R}^{n_{\text{dim}}}$ be the displacement field, assumed to be differentiable except possibly for jumps on \mathcal{S} .

In this model of solid mechanics and fracture, two potential energies exist, one associated with the bulk model and one with a network of surfaces \mathcal{S} inside the domain that serve as potential sites of fracture. Thus, the mechanical potential has the form:

$$\mathcal{E} = \int_{\Omega} \Psi(u) dV + \int_{\mathcal{S}} \Phi([u]) dS - \int_{\Omega} f \cdot u dV - \int_{\mathcal{S}_t} \tilde{t} \cdot u dS \quad (1)$$

*Supported in part by an NSERC Discovery Grant.

[†]Department of Combinatorics & Optimization, University of Waterloo, 200 University Ave. W., Waterloo, Ontario, N2L 3G1, Canada, vavasis@uwaterloo.ca.

[‡]Department of Applied Mathematics and Department of Mechanical & Mechatronics Engineering, University of Waterloo, 200 University Ave. W., Waterloo, Ontario, N2L 3G1, Canada, papoulia@uwaterloo.ca

[§]Department of Mechanical & Mechatronics Engineering, University of Waterloo, 200 University Ave. W., Waterloo, Ontario, N2L 3G1, Canada, mhirmand@uwaterloo.ca

where $[u]$ denotes the jump in u across the surface. Here, Ψ corresponds to the strain-energy density function while Φ corresponds to energy density of new surfaces (fracture). The final two terms correspond to body loads (f) and traction loads (\hat{t}) respectively, Here \mathcal{S}_t denotes the portion of $\partial\Omega$ with traction loads. Note that the use of a potential energy functional implies reversibility; we return to this matter below. Later on, we will add another term to the optimization formulation to account for momentum. In addition, we will impose displacement boundary conditions and inequality constraints. The latter will be used to model contact and a no-interpenetration requirement for the mesh.

We further stipulate that $\Phi([u])$ is a nondifferentiable function of $[u]$ when $[u] = 0$. As explained in [21], this is an essential ingredient of the formulation; see also Charlotte et al. [6] in a slightly different context. Because of the nondifferentiability at $[u] = 0$, no jumps in u will occur across any surface until a positive finite level of loading occurs.

The above model falls into the category of “cohesive zone” models [2, 24, 8] because it accounts for crack propagation with explicit representation of crack surfaces and an associated displacement-traction relation (which is obtained as a derivative of Φ for nonzero values of $[u]$). Furthermore, it falls into the category of “initially rigid” cohesive zone models because of the property that there is no crack opening until a specific positive finite load level is attained. Initially rigid models are preferred over the alternative “initially elastic” models in problems where the crack path is not known a priori. Inclusion of a network of initially elastic surfaces would lower the global stiffness of Ω ; as the number of crosscutting surfaces in \mathcal{S} tends to infinity, the global stiffness is driven to 0. In contrast, there is no limit to how much surface area may be encompassed by \mathcal{S} in (1) for the class of nondifferentiable potentials $\Phi([u])$ proposed in [21].

In [22], it was argued that unless significant care is taken in designing the algorithm, methods for initially rigid cohesive fracture are likely to be “time discontinuous.” The issue is that after space discretization, a system of ODE’s for nodal values of the displacement u and other quantities arises, i.e., a system of the form $du/dt = \mathbf{f}(u)$. The forcing function $\mathbf{f}(u)$ of these ODE’s is a discontinuous function of u , and this leads to nonconvergent or unreliable numerical methods. In [21] and also in this paper, the problems of time discontinuity are sidestepped because the modeling technique does not lead to a system of ODE’s—the usual step of passing to a weak form does not apply because the potential is nondifferentiable. Instead, the method involves time steps each of which corresponds to a physically based energy minimization operation.

The formulation (1) thus reduces the problem of modeling fracture to a sequence of optimization problems. These are infinite dimensional problems, but they are reduced to finite-dimensional optimization using finite element analysis as discussed in Section 3. This problem was solved in [21] using a continuation method. Hirmand and Papoulia [13] solve it using a Nitsche discontinuous Galerkin method (see also the related work by Radovitzky et al. [23]) in which the multipliers of the optimization problem are interpreted as stresses at the crack surface. The contribution of the present paper is a solution method for the optimization problem (1) using a novel interior-point method. A key step in the development, as explained in Section 4, is to recast a certain equation (namely, the second line of (11)) that appears in the optimization problem as an inequality (namely, the second line of (12)).

This technique is commonplace in the optimization literature but is new (as far as we know) to fracture mechanics. General background on interior-point methods is provided in Section 2. As mentioned earlier, the development of the formulation continues in Section 3, which explains our finite-element discretization. The method as described so far is reversible. Irreversibility may be incorporated via the additional dependence of Φ in (1) on a damage variable as detailed in Section 3.

The interior-point formulation is provided in Section 4. Most of the literature on interior-point methods relates to convex optimization. Our optimization problem is nonconvex, which requires modifications to the interior-point method compared to the previous literature as explained in Section 5. The interior-point method needs a feasible starting point; for this we rely on a technique developed in Section 6. Details of the computational procedure are spelled out in Section 7. Our computational experiments are described in Section 9; these experiments involve checking the balance of energy, the computation of which is described in Section 8. We conclude in Section 10 with an itemization of the development of the optimization models as well as the components of our computational method.

We conclude this section with a discussion of related literature. Other than Papoulia [21] and Hirmand

and Papoulia [13], the most closely related work is Lorentz’s [16] method, which also treats initially rigid fracture using a potential like (1) for the same reasons as us. Lorentz does not use an optimization method per se but rather considers the subdifferential of (1) as a generalization of a system of equations for generating a time step. Slightly more distantly related to the present work is the phase-field method of modeling fracture [5]. In this case, energy minimization is also invoked, but the functional pertains to a smeared crack location rather than a sharp surface. As a consequence, a sharp representation of the crack must be determined *a posteriori*, although some authors e.g., Geelen et al. [11], Wang and Waisman [28], have shown recently that a sharp representation of the crack can be directly coupled to a phase-field model.

2 Interior-point algorithms

In this section we present general background on interior-point methods. For more in-depth treatment, see, e.g., [30]. The application of these methods to initially rigid cohesive fracture is provided in Section 4.

A *closed convex cone* is defined to be a set $K \subset \mathbf{R}^n$ with the properties that (i) K is closed, (ii) K is convex, (iii) K is a cone, i.e., $\mathbf{x} \in K \Rightarrow \lambda \mathbf{x} \in K$ for all $\lambda \geq 0$, and (iv) $\mathbf{0} \in K$ (i.e., $K \neq \emptyset$).

Two important special examples of closed convex cones are $\mathbf{R}_n^+ = \{\mathbf{x} \in \mathbf{R}^n : x_i \geq 0 \forall i = 1, \dots, n\}$, the *nonnegative orthant*, and $C_2^n = \{\mathbf{x} \in \mathbf{R}^n : x_1 \geq \|\mathbf{x}(2:n)\|\}$, the *second-order cone*. Here, $\mathbf{x}(2:n)$ (Matlab notation) denotes the subvector of \mathbf{x} indexed by coordinates 2 through n .

The two cones mentioned in the previous paragraph both have standard *self-concordant barrier functions*. For \mathbf{R}_n^+ , the standard self-concordant barrier function is $\phi_{\text{NNO}}(\mathbf{x}) = -\sum_{i=1}^n \log(x_i)$. For C_2^n , the standard self-concordant barrier function is $\phi_{\text{SOC}}(\mathbf{x}) = -\frac{1}{2} \log(x_1^2 - x_2^2 - \dots - x_n^2)$. We regard these functions as taking on the value infinity outside the relevant cones. These functions have the property that they are strictly convex functions on the interior of their respective cones, and they tend to infinity as the boundary of the cone is approached. “Self concordance” involves two other technical properties; see [18].

If $K_1 \subset \mathbf{R}^{n_1}, \dots, K_r \subset \mathbf{R}^{n_r}$ are all closed convex cones with barrier functions ϕ_1, \dots, ϕ_r , then $K_1 \times \dots \times K_r$ is also a closed convex cone, and its barrier function is $\phi_1(\mathbf{x}_1) + \dots + \phi_r(\mathbf{x}_r)$ for $(\mathbf{x}_1, \dots, \mathbf{x}_r) \in K_1 \times \dots \times K_r$.

Consider the optimization problem

$$\begin{aligned} \min_{\mathbf{x}} \quad & f(\mathbf{x}) \\ \text{s.t.} \quad & \mathbf{g}(\mathbf{x}) = \mathbf{0}, \\ & \mathbf{x} \in K, \end{aligned}$$

where K is a closed convex cone that has a barrier function $\phi(\mathbf{x})$. This problem may be solved as follows. Let $\mu_1 \equiv \mu_{\text{init}}, \mu_2, \dots$ be a decreasing sequence of positive parameters tending to 0. Then for $k = 1, 2 \dots$ we solve

$$\begin{aligned} \min_{\mathbf{x}} \quad & f(\mathbf{x}) + \mu_k \phi(\mathbf{x}) \\ \text{s.t.} \quad & \mathbf{g}(\mathbf{x}) = \mathbf{0}, \end{aligned} \tag{2}$$

an equality-constrained optimization problem, and we define \mathbf{x}_k to be the optimizer or approximate optimizer. On iteration $k+1$, we use \mathbf{x}_k as the initial guess for the optimization algorithm, which is commonly Newton’s method. In other words, we iteratively solve a sequence of equality-constrained optimization problems. This method is called a *primal* or *primal-only* interior-point method.

The case most commonly studied in the literature is the case when $f(\mathbf{x})$ is the linear function $\mathbf{c}^T \mathbf{x}$ and convex and the equality constraints are linear: $\mathbf{g}(\mathbf{x}) \equiv \mathbf{A}\mathbf{x} - \mathbf{b}$ for some matrix \mathbf{A} and vector \mathbf{b} . In this case, there is an extensive theory guaranteeing convergence to a global optimizer for the above algorithm for a suitable sequence of weights μ_1, μ_2, \dots . See, e.g., [18].

We can also define a *primal-dual* method as follows. We first write the first-order (Lagrange or KKT) optimality condition for (2), which is,

$$\nabla f(\mathbf{x}^*) + \mu_k \nabla \phi(\mathbf{x}^*) + J(\mathbf{x}^*)^T \boldsymbol{\lambda} = \mathbf{0}, \tag{3}$$

where \mathbf{x}^* is the optimizer of (2), $J(\mathbf{x}^*)$ denotes the first derivative (Jacobian matrix) of $\mathbf{g}(\mathbf{x})$, and $\boldsymbol{\lambda}$ is the Lagrange multiplier.

Assume k in the previous item is fixed for now. In the case of $K = \mathbf{R}_+^n$ so that $\phi_{\text{NNO}}(\mathbf{x}) = -\sum_{i=1}^n \log(x_i)$ and

$$\nabla\phi(\mathbf{x}) = \begin{pmatrix} -1/x_1 \\ \vdots \\ -1/x_n \end{pmatrix},$$

we define dual variable $s_i = \mu_k/x_i$ for $i = 1, \dots, n$. Then the optimality condition (3), combined with feasibility and with a rearrangement of the definition of s_i yields the following system of equations:

$$\begin{aligned} \nabla f(\mathbf{x}) - \mathbf{s} + J(\mathbf{x})^T \boldsymbol{\lambda} &= \mathbf{0}, \\ \mathbf{g}(\mathbf{x}) &= \mathbf{0}, \\ x_i s_i &= \mu_k, \quad \forall i = 1, \dots, n. \end{aligned}$$

The final group of equations is called ‘‘complementarity’’. It may be rewritten $\mathbf{x} \circ \mathbf{s} = \mu_k \mathbf{e}$, where ‘‘ \circ ’’ is called the *Jordan product* for \mathbf{R}_+^n , and \mathbf{e} denotes the vector of all 1’s. The Jordan product is defined exactly as: the i th entry of $\mathbf{x} \circ \mathbf{s}$ is $x_i s_i$. This notation also implies that \mathbf{x}, \mathbf{s} are in the cone, i.e., $x_i \geq 0$ and $s_i \geq 0$ for all $i = 1, \dots, n$.

In the case of C_2^n , the gradient of the barrier function is

$$\nabla\phi_{\text{SOC}}(\mathbf{x}) = \begin{pmatrix} -x_1/d \\ x_2/d \\ \vdots \\ x_n/d \end{pmatrix},$$

where $d = x_1^2 - x_2^2 - \dots - x_n^2$. Then we define dual variables $s_1 = \mu_k x_1/d$, $s_2 = -\mu_k x_2/d$, \dots , $s_n = -\mu_k x_n/d$. Note that, assuming $\mathbf{x} \in C_2^n$, it also follows from these formulas that $\mathbf{s} \in C_2^n$. In this case, the optimality condition (3) plus feasibility and the definition of \mathbf{s} can be written:

$$\begin{aligned} \nabla f(\mathbf{x}) - \mathbf{s} + J(\mathbf{x})^T \boldsymbol{\lambda} &= \mathbf{0}, \\ \mathbf{g}(\mathbf{x}) &= \mathbf{0}, \\ \mathbf{x} \circ \mathbf{s} &= \mu_k \mathbf{e}. \end{aligned}$$

Here, for C_2^n , the Jordan product $\mathbf{x} \circ \mathbf{s}$ is defined by

$$(\mathbf{x} \circ \mathbf{s})_i = \begin{cases} \mathbf{x}^T \mathbf{s}, & i = 1, \\ x_1 s_i + s_1 x_i, & i = 2, \dots, n. \end{cases}$$

Here, $\mathbf{e} = [1, 0, \dots, 0]^T$. It can be checked that $\mathbf{x} \circ \mathbf{s} = \mu_k \mathbf{e}$ iff $s_1 = \mu_k x_1/d$ and $s_i = -\mu_k x_i/d$ for $i = 2, \dots, n$, where d is as above, provided that $\mathbf{x}, \mathbf{s} \in C_2^n$.

Finally, if K_1, \dots, K_r are all convex cones each with a Jordan product and with Jordan identities $(\mathbf{e}_1, \dots, \mathbf{e}_r)$, then the Jordan identity for $K_1 \times \dots \times K_r$ is $(\mathbf{e}_1, \dots, \mathbf{e}_r)$ and the Jordan product is elementwise: $(\mathbf{x}_1, \dots, \mathbf{x}_r) \circ (\mathbf{s}_1, \dots, \mathbf{s}_r) = (\mathbf{x}_1 \circ \mathbf{s}_1, \dots, \mathbf{x}_r \circ \mathbf{s}_r)$.

The *primal-dual interior-point method* consists of solving the system of nonlinear equations:

$$\begin{aligned} \nabla f(\mathbf{x}) - \mathbf{s} + J(\mathbf{x})^T \boldsymbol{\lambda} &= \mathbf{0}, \\ \mathbf{g}(\mathbf{x}) &= \mathbf{0}, \\ \mathbf{x} \circ \mathbf{s} &= \mu_k \mathbf{e}, \end{aligned}$$

whose variables are $(\mathbf{x}, \boldsymbol{\lambda}, \mathbf{s})$, using Newton’s method for a sequence of decreasing μ_k ’s, and using the converged (or approximately converged) solution $(\mathbf{x}_{k-1}, \boldsymbol{\lambda}_{k-1}, \mathbf{s}_{k-1})$ as the starting guess for the k th iteration. If Newton’s method is applied directly to the above system, this yields a step called the AHO direction (Alizadeh-Haeberly-Overton). See [27] for an in-depth discussion.

In the nonconvex case, the known theorems are considerably weaker. An analysis of a primal-dual interior-point method for nonconvex second-order cone programming is presented by Yamashita and Yabe [29]. The main innovation in that work is a merit function that ensures convergence. We have experimented with a primal-dual interior point method but have not used it herein because it sometimes failed to converge to a solution and instead became trapped close to a boundary of the feasible region. The hypotheses of the Yamashita-Yabe method do not hold for the problem herein. Therefore, the method used in our solver is a primal-only method. However, we use the primal-dual formulation in the computations of energy balance detailed below in Section 8.

3 Finite element discretization

As mentioned earlier, we assume a physical domain $\Omega \subset \mathbf{R}^{n_{\text{dim}}}$ ($n_{\text{dim}} = 2$ or $n_{\text{dim}} = 3$), which is the closure of an open, bounded set with a piecewise smooth boundary. In this section, we describe the notation used to define a finite-element discretization of Ω and u . Assume that Ω is meshed with a triangulation \mathcal{T} . The triangulation is assumed to be simplicial, although the method can be extended to meshes with hanging nodes. The n_{dim} -dimensional elements of this mesh are referred to as *bulk elements*.

As mentioned in the introduction, we further assume that Ω contains a union \mathcal{S} of curves or surfaces to represent possible crack paths. For the remainder of this work, we take \mathcal{S} to be the union of nonexterior bounding curves or surfaces of the bulk elements. The cohesive method inserts *interface elements* along triangle edges ($n_{\text{dim}} = 2$) or facets ($n_{\text{dim}} = 3$) for every pair of adjacent bulk elements. Let the size of \mathcal{S} (number of curves or facets) be denoted n_e . Each bulk element has its own nodes, i.e., no node belongs to more than one bulk element. Two adjacent bulk elements $t_1, t_2 \in \mathcal{T}$ that border on the same interface element e each have nodes in common with e . Therefore, the connectivity of the mesh is determined by nodes shared between bulk and interface elements. Let n_0 denote the total number of nodes of bulk elements. Let n_x denote the number of nodal degrees of freedom not constrained by displacement or velocity boundary conditions. Thus, $n_x \leq n_{\text{dim}}n_0$.

On each time step, an optimization problem is solved to determine the displacements at the midpoint of the time interval. For the rest of this discussion, assume the time step is fixed so that we omit the subscript for time. Let $\mathbf{u} \in \mathbf{R}^{n_{\text{dim}}n_0}$ be the vector of all nodal displacements (n_{dim} coordinate entries for each of n_0 nodes). As in [21], this value of \mathbf{u} plays the role of the unknown at the midpoint of a time-step.

Let $\mathbf{x} \in \mathbf{R}^{n_x}$ reparameterize \mathbf{u} : \mathbf{x} stands for the degrees of freedom associated with unconstrained nodal displacements. The relationship between \mathbf{u} and \mathbf{x} is as follows. There is a fixed $n_{\text{dim}}n_0 \times n_x$ matrix R such that $\mathbf{u} = R\mathbf{x} + \mathbf{u}_{BC}$. Here, \mathbf{u}_{BC} is the $n_{\text{dim}}n_0$ -vector that carries information about displacement boundary conditions. Note that \mathbf{u}_{BC} will depend on the time-step index in the case of velocity boundary conditions.

The strain energy associated with a bulk element $t \in \mathcal{T}$ is given by an elastic or hyperelastic energy functional. For example, in the $n_{\text{dim}} = 2$ case, one choice for the energy is the one proposed by Knowles and Sternberg [14] for plane stress given by

$$\Psi(u) = c_1 [\text{Tr}(C) + \mathcal{J}^{-2\beta}(1 + 1/\beta)] \quad (4)$$

where Tr stands for the trace operator, $\mathcal{J} = \det(C)^{(1+1/\beta)/2}$, $C = F^T F$ (Cauchy-Green strain), F is the (2-dimensional) displacement gradient, c_1, β are material constants. Inelastic bulk material behavior is not considered herein.

The strain energy in the bulk is discretized as a function $b_0(\mathbf{u})$ using quadrature over elements of \mathcal{T} , i.e.,

$$b_0(\mathbf{u}) = \int_{\Omega} \Psi(u_h) dV,$$

where u_h is the finite-element interpolant specified by nodal values in the vector \mathbf{u} . This function $b_0(\mathbf{u})$ is rewritten as $b(\mathbf{x})$ (i.e., $b(\mathbf{x}) \equiv b_0(R\mathbf{x} + \mathbf{u}_{BC})$).

The momentum energy term $m_0(\mathbf{u})$ arising from the implicit midpoint rule is derived in [21] to be

$$m_0(\mathbf{u}) = \frac{2}{\Delta t^2} (\mathbf{u} - \mathbf{u}^i - \mathbf{v}^i \Delta t/2)^T M (\mathbf{u} - \mathbf{u}^i - \mathbf{v}^i \Delta t/2),$$

where Δt is the time step, M is the $n_{\text{dim}}n_0 \times n_{\text{dim}}n_0$ positive definite mass matrix, and \mathbf{u}^i and \mathbf{v}^i are displacement and velocity vectors from the preceding time step. Define $m(\mathbf{x}) = m_0(R\mathbf{x} + \mathbf{u}_{BC})$. This may be loosely regarded as the discretization of kinetic energy; see [21] for a more precise explanation. Note that $m(\mathbf{x})$ is a convex quadratic function of \mathbf{x} .

Next, define an interface potential to stand for the second term of (1) as in [21]. This potential for a given element edge/surface $e \in \mathcal{S}$ is

$$\int_{\eta \in \Delta} g(\delta(\theta_e(\eta)); d(\theta_e(\eta))) \theta'_e(\eta) d\eta \quad (5)$$

where θ_e parameterizes the edge/surface e with parameter η (a scalar for $n_{\text{dim}} = 2$; a 2-vector for $n_{\text{dim}} = 3$) which lies in a reference domain Δ , $\delta(\cdot)$ is the *effective opening displacement* as calculated from displacement jump in the element boundaries, g is the interface energy function and d is a damage variable discussed below. We follow the commonplace definition similar to Ortiz and Pandolfi [20]:

$$\delta(x) = \sqrt{[u_n(x)]^2 + (\beta^{\text{MIX}})^2 \|[u_s(x)]\|^2}, \quad (6)$$

where $u_n(\cdot)$ and $u_s(\cdot)$ are the normal and tangential opening displacements at a point $x \in \Omega$ that lies on an interface. We return to these functions below. Here, β^{MIX} is a material constant called the *mixity parameter*. Thus, the second term $\Phi([u])$ of (1) is the composition of the function $g(\delta; d)$ appearing in (5) with the function $\delta([u])$ appearing in (6). The dependence on d is discussed below.

The simplest physically reasonable choice for g prior to the introduction of damage is:

$$g(\delta) = \begin{cases} l\delta + q\delta^2, & \delta \in [0, \delta_u] \\ l\delta_u + q\delta_u^2, & \delta \geq \delta_u, \end{cases} \quad (7)$$

where δ_u , the ultimate opening displacement, is a material parameter; quadratic coefficient $q = -\sigma_c/(2\delta_u)$, $l = \sigma_c$, and σ_c , the critical traction, is another material parameter. One checks that with these formulas, g is a piecewise C^1 (continuous function and first derivative) quadratic function. Its first derivative with respect to δ , g' , is therefore piecewise linear and continuous. With these choices of the three parameters, $g'(0) = \sigma_c$, indicating that the initial traction (first derivative of energy with respect to δ) is σ_c . The area under the curve of the plot of $g'(\delta)$ is $G_c = \sigma_c\delta_u/2$, a material parameter called the ‘‘critical energy release rate’’. (Note: of the three material parameters σ_c, δ_u, G_c , only two can be chosen independently as the previous equality demonstrates.)

We now extend this formula to include a nonnegative scalar damage parameter d , initially equal to 0. The role of scalar d is to model irreversible damage to the interface. As in [20] and many other previous works, we define this parameter equal to the maximum opening displacement (not exceeding δ_u) encountered over previous time values. When $d = \delta_u$, the interface has no remaining cohesion. The extended formula is:

$$g(\delta; d) = \begin{cases} l(d)\delta, & \delta \in [0, d], \\ l(d)\delta + q(\delta - d)^2 & \delta \in [d, \delta_u], \\ l(d)\delta_u + q(\delta_u - d)^2 & \delta > \delta_u, \end{cases} \quad (8)$$

where now $q = -\sigma_c/(2\delta_u)$, $l(d) = -2(\delta_u - d)q$. When $d = 0$, the formula in the previous paragraph is recovered. See Fig. 1. Unlike previous works such as [20], this formula implies that the material retains a residual critical stress when $0 < d < \delta_u$. In contrast, most previous works specify that after the onset of damage, the interface behaves like an initially elastic interface (i.e., unloads to the origin). The difference in practice between the two models appears to be minor, but our formulation has the mathematical advantage that it prevents a pathological situation in which the second derivative of g can have an unboundedly large value.

In the finite element approximation, the integral (5) is computed for each edge ($n_{\text{dim}} = 2$) or facet ($n_{\text{dim}} = 3$) with a n_g -point Gauss quadrature rule. Let $n_i = n_e n_g$ stand for the total number of Gauss-points of interfaces. Let us introduce a new variable $\mathbf{s}_0 \in \mathbf{R}^{n_i}$ that represents the effective opening displacements

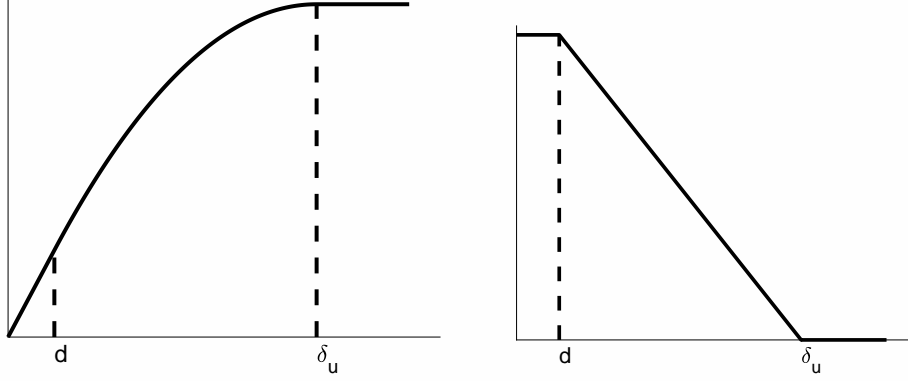


Figure 1: Plot of the function $g(\delta; d)$ (left) and $g'(\delta; d)$ (right) defined by (8). Although difficult to discern at this scale, the segment of the curve on the left corresponding to abscissas lying in $[0, d]$ is straight (linear).

at the Gauss points. In other words, \mathbf{s}_0 stores the vector of values of $\delta(\theta_e(\eta_\iota))$, $\iota = 1, \dots, n_g$, described above at each Gauss point $\eta_1, \dots, \eta_{n_g}$ of each interface e . Then the potential due to interfaces is written

$$h(\mathbf{s}_0; \mathbf{d}) = \sum_e \sum_{\iota=1}^{n_g} \omega_{e,\iota} g((s_0)_{e,\iota}; d_{e,\iota}); \quad (9)$$

this is the finite-element approximation to $\Phi([u])$ that appears in (1). We have associated a damage variable $d_{e,\iota}$ for $e \in \mathcal{S}$ and $\iota = 1, \dots, n_g$, i.e., one for each of the n_i interface Gauss points, that indicate the level of damage. Here, $\omega_{e,\iota}$ is the quadrature weight. This function h is separable in the entries of \mathbf{s}_0 , and hence its Hessian is a diagonal matrix.

Let $\mathbf{s}_1 \in \mathbf{R}^{n_i}$ denote the normal opening displacement. Let $\mathbf{s}_2, \dots, \mathbf{s}_{n_{\text{dim}}} \in \mathbf{R}^{n_i}$ stand for the tangential opening displacements scaled by β^{MIX} . (Note that for three-dimensional problems, there is not a unique way to define a tangential coordinate system at each point on an interface. Any method for defining tangential coordinates is acceptable provided that it is applied consistently for the duration of the solution procedure.) Next, we revisit (6). First, the left-hand side is needed only at the Gauss points of the interfaces. In this case, the left-hand side is just $(s_0)_{e,\iota}$. A similar substitution may be made on the right-hand side, so this constraint is rewritten as

$$(s_0)_{e,\iota} = \sqrt{(s_1)_{e,\iota}^2 + \dots + (s_{n_{\text{dim}}})_{e,\iota}^2},$$

for $e = 1, \dots, n_e$, $\iota = 1, \dots, n_g$. Observe that this constraint is nondifferentiable at the origin, that is, when for some e, ι , $(s_1)_{e,\iota} = \dots = (s_{n_{\text{dim}}})_{e,\iota} = 0$. This nondifferentiability is fundamental to the model and is precisely the reason why it is able to capture the initially rigid interface behavior. A detailed explanation of the role of this nondifferentiability is provided in [21].

The vectors $\mathbf{s}_1, \dots, \mathbf{s}_{n_{\text{dim}}}$ containing the components of the opening displacements are functions of the displacements stored in \mathbf{u} . In other words, we can determine entries of $\mathbf{s}_1, \dots, \mathbf{s}_{n_{\text{dim}}}$ by evaluating jumps of displacements interpolated from shape functions. As mentioned earlier, we have reparameterized \mathbf{u} by \mathbf{x} . Therefore we can define geometric functions $c_{k,e,\iota}$ such that

$$(s_k)_{e,\iota} = c_{k,e,\iota}(\mathbf{x}), \quad (10)$$

for $k = 1, \dots, n_{\text{dim}}$, $e = 1, \dots, n_e$, $\iota = 1, \dots, n_g$. As observed in [21], these functions are nonlinear because of geometric nonlinearity, namely, the normal and tangent directions depend on the current values of the displacements. In addition to geometry, the functions $c_{2,e,\iota}, \dots, c_{n_{\text{dim}},e,\iota}$ also have the mixity factor β^{MIX} encoded in them.

As mentioned in the introduction, one advantage of the interior-point formulation is the ability to handle conic convex constraints essentially for free. One special case of conic convex constraints is linear inequality constraints. Let us assume that the system has additional linear constraints of the form $E\mathbf{x} \geq \mathbf{a}$. (Later on, we will use these inequalities to model a simple form of a contact constraint.) Here, $E \in \mathbf{R}^{n_{\text{LI}} \times n_x}$ is a known matrix and $\mathbf{a} \in \mathbf{R}^{n_{\text{LI}}}$ is a known vector, both of which may vary from one time-step to the next, and n_{LI} denotes the number of linear inequality constraints.

Thus, the optimization problem to solve for one time-step in the model of cohesive fracture is:

$$\begin{aligned} \min_{\mathbf{x}, \mathbf{s}_0, \mathbf{s}_1, \dots, \mathbf{s}_{n_{\text{dim}}}} \quad & m(\mathbf{x}) + b(\mathbf{x}) + h(\mathbf{s}_0; \mathbf{d}) + \mathbf{f}^T \mathbf{x} \\ \text{s.t.} \quad & (s_0)_{e,\ell} = \sqrt{(s_1)_{e,\ell}^2 + \dots + (s_{n_{\text{dim}}})_{e,\ell}^2} \quad \forall e, \ell, \\ & (s_k)_{e,\ell} = c_{k,e,\ell}(\mathbf{x}) \quad \forall k = 1, \dots, n_{\text{dim}}, \forall e, \ell, \\ & E\mathbf{x} \geq \mathbf{a}, \\ & (s_1)_{e,\ell} \geq 0 \quad \forall e, \ell. \end{aligned} \quad (11)$$

The terms in the objective have already been discussed except for the last term, which stands for the sum of traction and body forces from (1). The first, second and third constraints were already discussed. The fourth prevents interpenetration between neighboring elements.

4 Interior-point method for fracture

A key modification to (11) that makes it amenable to an interior-point method is to replace the first equality constraint with an inequality constraint:

$$\begin{aligned} \min_{\mathbf{x}, \mathbf{s}} \quad & m(\mathbf{x}) + b(\mathbf{x}) + h(\mathbf{s}_0; \mathbf{d}) + \mathbf{f}^T \mathbf{x} \\ \text{s.t.} \quad & (s_0)_{e,\ell} \geq \sqrt{(s_1)_{e,\ell}^2 + \dots + (s_{n_{\text{dim}}})_{e,\ell}^2} \quad \forall e, \ell, \\ & (s_k)_{e,\ell} = c_{k,e,\ell}(\mathbf{x}) \quad \forall k = 1, \dots, n_{\text{dim}}, \forall e, \ell, \\ & E\mathbf{x} \geq \mathbf{a}, \\ & (s_1)_{e,\ell} \geq 0 \quad \forall e, \ell. \end{aligned} \quad (12)$$

Replacing the equality by an inequality constraint does not change the optimizer because h is a nondecreasing function of \mathbf{s}_0 . (In fact, it is perturbed to a strictly increasing function as described below.) This implies that the optimal solution to (12) satisfies $(s_0)_{e,\ell} = \sqrt{(s_1)_{e,\ell}^2 + \dots + (s_{n_{\text{dim}}})_{e,\ell}^2}$.

The benefit of this change is that an equality constraint of the form $(s_0)_{e,\ell} = \|(\mathbf{s}_{1:n_{\text{dim}}})_{e,\ell}\|$ defines a nonconvex set with a complicated (nonmanifold) structure, whereas the constraint $(s_0)_{e,\ell} \geq \|(\mathbf{s}_{1:n_{\text{dim}}})_{e,\ell}\|$ defines a convex set $C_2^{n_{\text{dim}}+1}$, the second-order cone. Here, $(\mathbf{s}_{1:n_{\text{dim}}})_{e,\ell}$ is the vector in $\mathbf{R}^{n_{\text{dim}}}$ whose entries are $((s_1)_{e,\ell}, \dots, (s_{n_{\text{dim}}})_{e,\ell})$.

As discussed in Section 2, the primal-only interior-point method replaces the inequality constraints in the preceding formulation with log-barrier terms. The parameter $\mu > 0$ starts at a large value and decreases to close to zero. This leads to the following formulation:

$$\begin{aligned} \min_{\mathbf{x}, \mathbf{s}} \quad & m(\mathbf{x}) + b(\mathbf{x}) + h_\mu(\mathbf{s}_0; \mathbf{d}) + \mathbf{f}^T \mathbf{x} + \mu \phi_{\text{NNO}}(E\mathbf{x} - \mathbf{a}) \\ & + \mu \sum_{e=1}^{n_e} \sum_{\ell=1}^{n_\ell} \zeta_{e,\ell} [\phi_{\text{SOC}}((\mathbf{s}_{0:n_{\text{dim}}})_{e,\ell}) + \phi_{\text{NNO}}((s_1)_{e,\ell})] \\ \text{s.t.} \quad & (s_k)_{e,\ell} = c_{k,e,\ell}(\mathbf{x}) \quad \forall k = 1, \dots, n_{\text{dim}}, \forall e, \ell. \end{aligned} \quad (13)$$

The positive weight $\zeta_{e,\ell}$ is defined by (15) in the next section. In addition, we have perturbed h of (12) to h_μ in (13), which is defined by (16) in the next section. As $\mu \rightarrow 0$, $h_\mu \rightarrow h$, thus recovering the original problem.

This formulation still contains equality constraints, but they are easily eliminated via substitution. In particular, we substitute $c_{k,e,\ell}(\mathbf{x})$ for $(s_k)_{e,\ell}$ (as in (10)) thus eliminating $(s_k)_{e,\ell}$, $k = 1, \dots, n_{\text{dim}}$, $e =$

$1, \dots, n_e, \iota = 1, \dots, n_g$. This elimination leaves the following unconstrained problem:

$$\begin{aligned} \min_{\mathbf{x}, \mathbf{s}_0} \quad & m(\mathbf{x}) + b(\mathbf{x}) + h_\mu(\mathbf{s}_0; \mathbf{d}) + \mathbf{f}^T \mathbf{x} + \mu \phi_{\text{NNO}}(E\mathbf{x} - \mathbf{a}) \\ & + \mu \sum_{e=1}^{n_e} \sum_{\iota=1}^{n_g} \zeta_{e,\iota} \left[\phi_{\text{SOC}}((s_0)_{e,\iota}, \mathbf{c}_{1:n_{\text{dim}},e,\iota}(\mathbf{x})) \right. \\ & \left. + \phi_{\text{NNO}}(c_{1,e,\iota}(\mathbf{x})) \right] \end{aligned} \quad (14)$$

The interior-point code solves (14) via a trust-region method. This is a standard technique to extend Newton’s method to nonconvex (unconstrained) optimization. More details on the method are in Section 7.

5 Sources of nonconvexity

The optimization problem (12) contains three sources of nonconvexity as follows. The bulk energy $b(\mathbf{x})$ is nonconvex in the displacements for nonlinear hyperelasticity, $h(\mathbf{s}_0; \mathbf{d})$ is nonconvex in \mathbf{s}_0 due to the negative coefficient of the quadratic term in (8), and the constraints $(s_i)_{e,\iota} = c_{i,e,\iota}(\mathbf{x})$, $i = 1, \dots, n_{\text{dim}}$, are nonlinear. (Note that in passing from (11) to (12), a fourth source of nonconvexity was eliminated by replacing an equality with an inequality.) Of these three sources, the nonconvexity of h is the most challenging to handle, and it is also the most fundamental to the application. Convexity of $b(\mathbf{x})$ could be recovered by adopting a simpler mechanical model such as linear elasticity. Linearity in the constraint $(s_k)_{e,\iota} = c_{k,e,\iota}(\mathbf{x})$ could be recovered by simply assuming that the normal vectors to the interfaces are determined by the initial rather than current configuration. There is, however, no apparent way to replace or approximate h with a convex function because g must have a nonconvex form similar to the form depicted in Fig. 1(left) to be physically meaningful.

Interior-point methods for nonconvex problems are considerably more delicate than for convex problems, and we were required to implement several stabilization methods in the interior-point framework to cope with the nonconvexity of h , which are as follows.

1. The interior-point method converges significantly faster if we weight the log-barrier terms for the constraints associated with interfaces by a factor proportional to their “local” length. In particular, we introduced weight $\zeta_{e,\iota}$ in (13), which is defined as

$$\zeta_{e,\iota} = 10^4 G_c \omega_{e,\iota}, \quad (15)$$

where $\omega_{e,\iota}$ is the quadrature weight in (9). Using a weight proportional to $\omega_{e,\iota}$ is physically natural because it means, for example, that the contribution to the barrier function from an interface is invariant (up to discretization error) if the interface is subdivided into smaller pieces. Making the weight proportional to G_c , the critical energy release rate, is also natural since the other terms in the objective function stand for work or energy quantities. Weighting is not necessary (and is typically not even considered) in the case of convex interior-point methods.

2. On intermediate stages of the interior-point method, the interfaces are favored to open by the log-barrier term associated with the constraint $(s_1)_{e,\iota} \geq 0$ when μ is large. Without extra measures, they can open by more than δ_u , in which case their traction is 0 and they no longer hold the body together. Their traction is not recovered as μ is decreased due to the nonconvexity of h . For this reason, a quadratic regularization term is added to the cohesive traction. This term has the form

$$(5 \cdot 10^5) \alpha \omega_{e,\iota} \max(1 - d_{e,\iota}/\delta_u, 8 \cdot 10^{-6}) (s_0)_{e,\iota}^2,$$

where $\alpha > 0$ is a small scalar, $\omega_{e,\iota}$ is the quadrature weight in (9), $d_{e,\iota}$ is the damage value, $(s_0)_{e,\iota}$ is the (unknown) effective opening displacement of Gauss point ι of the interface e . From now on, we denote:

$$h_\alpha(\mathbf{s}_0; \mathbf{d}) = h(\mathbf{s}_0; \mathbf{d}) + \sum_{e,\iota} (5 \cdot 10^5) \alpha \omega_{e,\iota} \max(1 - d_{e,\iota}/\delta_u, 0.000008) (s_0)_{e,\iota}^2, \quad (16)$$

As already noted in (14), the method sets α in (16) equal to the barrier parameter μ (so that the original problem is recovered as $\mu \rightarrow 0$).

3. The Newton step associated with the interior-point step is not always well defined because the Hessian may not be positive definite. To address this problem, we use a common regularization to extend Newton to nonconvex optimization, namely, the trust-region method. Some modifications to the standard trust-region method were necessary for this application; these are described in detail in Section 7.

The net effect of these stabilization techniques is that the method is reasonably fast and robust on all the computational experiments tried so far.

6 Attaining feasibility with “Phase I” initialization

An issue to address is that interior-point methods for optimization require an interior starting point. There are so-called “infeasible” interior-point methods that ease this restriction, but the theory for such methods in the case of nonconvex problems is not well developed, and in practice they can be difficult to use. A natural choice for initialization is the converged solution for the previous time step, but such a solution may violate the inequality constraints such as contact. In addition, for moving displacement boundary conditions (i.e., velocity boundary conditions), the boundary nodes must be displaced each iteration to new positions to attain feasibility. Depending on the magnitude of the velocity, this can cause elements along the boundary to become inverted or nearly inverted, which makes the bulk material model behave poorly to the extent that recovering a noninverted shape is unattainable with Newton’s method.

One solution to the problem described in the last paragraph is to take small load steps, thus limiting the degree of misshapeness among boundary elements. The drawback of this technique is that it makes the time-step dependent on the mesh size because a finer mesh implies that a smaller boundary distortion can be tolerated. Recall that the method proposed herein is an implicit method. A big advantage of implicit methods is exactly that the time step and mesh size can be chosen independently. Thus, coping with moving boundaries by subdividing time-steps undermines one of the main benefits of implicit methods.

An alternative approach, adopted here, is to start with a so-called “Phase I” initialization. During Phase I, the optimization problem is modified with a new variable t constrained $t \geq 0$ and a “big M ” term in the objective. A preliminary version of the modified problem is as follows.

$$\begin{aligned} \min_{\mathbf{x}, \mathbf{s}_0, t} \quad & m(\mathbf{x}) + b(\mathbf{x}) + h_{\mu_{\text{init}}\sqrt{M}}(\mathbf{s}_0; \mathbf{d}) + \mathbf{f}^T \mathbf{x} + Mt \\ & + \mu_{\text{init}}\phi_{\text{NNO}}(\mathbf{E}\mathbf{x} + t\mathbf{e} - \mathbf{a}) + \mu_{\text{init}}\phi_{\text{NNO}}(t) \\ & + \mu_{\text{init}} \sum_{e=1}^{n_e} \sum_{\iota=1}^{n_g} \zeta_{e,\iota} \left[\phi_{\text{SOC}}((s_0)_{e,\iota}, \mathbf{c}_{1:n_{\text{dim}},e,\iota}(\mathbf{x})) \right. \\ & \left. + \phi_{\text{NNO}}(\mathbf{c}_{1,e,\iota}(\mathbf{x}) + t\mathbf{e}) \right] \end{aligned} \quad (17)$$

Here, \mathbf{e} is the vector of all 1’s. Note that during Phase I, μ is held at its initial value as suggested by the notation μ_{init} appearing in (17).

The rationale for (17) is as follows. The variable t can be initialized to a large positive value, which ensures that the barrier functions $\phi_{\text{NNO}}(\cdot)$ have positive arguments in all occurrences. In addition, the variables $(s_0)_{e,\iota}$ can be initialized to sufficiently large values for all interface Gauss points (e, ι) to ensure that the argument of ϕ_{SOC} is feasible. Thus, except for the issue of element inversion that is discussed below, it is straightforward to find an initial feasible point for (17). On the other hand, at the optimizer for (17), $t > 0$ will be a relatively small value because the term Mt in the objective function penalizes a large t . If a feasible solution to (17) has a small value of $|t|$, then we can simply set $t = 0$ and expect to have a feasible solution for (14).

If the solution so obtained is feasible for (14), then we proceed to a solver for (14) using this initial guess. If not, we re-solve (17) with M increased by a factor of 8 (initially, $M = 64$). A larger value of M means a smaller value of $t > 0$ at the optimizer. The parameter α appearing in h_α in (16) is $\mu_{\text{init}}\sqrt{M}$ in order to ensure that the quadratic penalty term in h is not swamped by the Mt term in the objective.

The “big- M ” technique thus handles feasibility of the barrier functions. Next, we further modify (17) to prevent element inversion that can be caused by moving boundary conditions. Recall that the vector of all degrees of freedom (DOFs) \mathbf{u} is parameterized by $\mathbf{u} = R\mathbf{x} + \mathbf{u}_{\text{BC}}$, where \mathbf{u}_{BC} carries the prescribed displacements and R is a fixed matrix. There is always a mathematically equivalent way to write the boundary constraints as $B\mathbf{u} = \mathbf{b}$, i.e., linear equations that must be satisfied by \mathbf{u} . The transformation from $(R, \mathbf{u}_{\text{BC}})$ to (B, \mathbf{b}) can be carried out using standard numerical linear algebra such as QR factorization. Note that both \mathbf{u}_{BC} and \mathbf{b} may depend on the time step τ , whereas R and B are fixed throughout the computation.

In Phase I, we let the vector of unknown displacements be \mathbf{u} rather than \mathbf{x} . Instead of equality constraints $B\mathbf{u} = \mathbf{b}$, we introduce two inequalities $B\mathbf{u} + t\mathbf{e} \geq \mathbf{b}$ and $B\mathbf{u} - t\mathbf{e} \leq \mathbf{b}$, where t is the Phase-I artificial variable. In turn, these two constraints are replaced by additional terms in the barrier objective function of the form $\mu\phi_{\text{NNO}}(B\mathbf{u} + t\mathbf{e} - \mathbf{b})$ and $\mu\phi_{\text{NNO}}(-B\mathbf{u} + t\mathbf{e} + \mathbf{b})$. Thus, the problem is reformulated as:

$$\begin{aligned} \min_{\mathbf{u}, \mathbf{s}_0, t} \quad & m_0(\mathbf{u}) + b_0(\mathbf{u}) + h_{\mu_{\text{init}}\sqrt{M}}(\mathbf{s}_0; \mathbf{d}) + \mathbf{f}_0^T \mathbf{u} + Mt \\ & + \mu_{\text{init}}\phi_{\text{NNO}}(E_0\mathbf{u} + t\mathbf{e} - \mathbf{a}_0) + \mu_{\text{init}}\phi_{\text{NNO}}(t) \\ & + \mu_{\text{init}}\phi_{\text{NNO}}(B\mathbf{u} + t\mathbf{e} - \mathbf{b}) + \mu_{\text{init}}\phi_{\text{NNO}}(-B\mathbf{u} + t\mathbf{e} + \mathbf{b}) \\ & + \mu_{\text{init}} \sum_{e=1}^{n_e} \sum_{\iota=1}^{n_g} \zeta_{e,\iota} \left[\phi_{\text{SOC}}((s_0)_{e,\iota}, \mathbf{c}_{0;1:n_{\text{dim},e,t}}(\mathbf{u})) \right. \\ & \left. + \phi_{\text{NNO}}(c_{0;1,e,\iota}(\mathbf{u}) + t\mathbf{e}) \right] \end{aligned} \quad (18)$$

Here, we recall the notation introduced earlier that $b_0(R\mathbf{x} + \mathbf{u}_{\text{BC}}) \equiv b(\mathbf{x})$ and similarly for $m_0(\cdot)$, \mathbf{f}_0 , E_0 , \mathbf{a}_0 , $\mathbf{c}_0(\cdot)$. Now it is apparent that by selecting both t and $(s_0)_{e,\iota}$ sufficiently large, all barrier constraints are feasible and no element is inverted by the initial guess for \mathbf{u} (the solution from the previous time-step). It is also apparent that if t is driven to a sufficiently small positive number by optimization on (18), then a feasible solution for the original (phase II) problem is obtained.

7 Computational procedure

In this section, we provide further details of the computational procedure of the cohesive solver. As mentioned in the last section, during Phase I, the displacement boundary conditions are enforced as inequalities, and therefore the vector of unknowns for the displacements in (18) is \mathbf{u} rather than \mathbf{x} . Let Π_τ be the linear projection that maps \mathbf{u} to \mathbf{x} , i.e., $\Pi_\tau(\mathbf{u}) = \operatorname{argmin}_{\mathbf{x}} \|(R\mathbf{x} + \mathbf{u}_{\text{BC},\tau}) - \mathbf{u}\|$, where τ is the time step. The feasibility test that terminates Phase I that was described in the previous section in more detail is: apply Π_τ to \mathbf{u} that solves (18) to make sure that the vector \mathbf{x} thus obtained is feasible for the main phase.

For the purpose of notation in the solvers, let $\boldsymbol{\xi}$ denote the concatenation $(\mathbf{x}, \mathbf{s}_0)$, the variables of the interior method (14), or $\bar{\boldsymbol{\xi}} = (\mathbf{u}, \mathbf{s}_0, t)$ in the case of Phase I when (18) is solved.

In the algorithms that follow, these variables $\boldsymbol{\xi}$ and $\bar{\boldsymbol{\xi}}$ are not meant to stand for new independent program variables but merely notational shorthand. For example, if \mathbf{x} is updated in a code that follows, then $\boldsymbol{\xi}$ is also updated implicitly since $\boldsymbol{\xi}$ contains \mathbf{x} as a subvector.

We make the following observation: given a value of \mathbf{x} or \mathbf{u} , it is possible to efficiently compute the optimal extension of \mathbf{x} to $\boldsymbol{\xi}$ or \mathbf{u} to $\bar{\boldsymbol{\xi}}$, where “optimal” in this context means minimizing the relevant objective function f . One observes from (12) that once \mathbf{x} is specified, the remaining variables $(s_0)_{e,\iota}$, $e = 1, \dots, n_e$, $\iota = 1, \dots, n_g$ and t (in the case of $\bar{\boldsymbol{\xi}}$) are decoupled and may be optimized individually using a univariate procedure (e.g., bisection). Let us denote these optimal values as $\boldsymbol{\xi}^*(\mathbf{x})$, $\bar{\boldsymbol{\xi}}^*(\mathbf{u})$.

The top-level procedure is described in Fig. 2. Every third time step, the algorithm computes matrices H_{μ_i} for $i = 1, \dots, n_\mu$, which are positive definite matrices used in the trust-region method.

The variables maintained in the main loop from one time step to the next are \mathbf{u} and \mathbf{d} , which are superscripted with the time step index τ . As discussed earlier, \mathbf{u} (or \mathbf{x}) encodes the displacements while \mathbf{d} is the damage state, which is updated from the displacements computed on each step.

```

From initial conditions determine initial guess for  $\mathbf{u}^0$ .
 $\mathbf{d}^0 := \mathbf{0}$ .
 $\{H_\mu\}_\mu := 0 \forall \mu$ ;  $H^{\text{PHASE1}} := 0$ .
for  $\tau := 1, \dots, n_{\text{step}}$ 
  if  $\text{rem}(\tau, 3) == 1$ 
     $H^{\text{PHASE1}}, \{H_\mu\}_\mu = \text{solver}(\tau, \mathbf{u}^0, \mathbf{d}^0, H^{\text{PHASE1}}, \{H_\mu\}_\mu, \text{PREPROCESS})$ .
  end if
   $\mathbf{u}^\tau := \text{solver}(\tau, \mathbf{u}^{\tau-1}, \mathbf{d}^{\tau-1}, H^{\text{PHASE1}}, \{H_\mu\}_\mu, \text{ORDINARY})$ .
  Compute  $\mathbf{d}^\tau$  from  $\mathbf{d}^{\tau-1}, \mathbf{u}^\tau$ .
end for

```

Figure 2: Top-level procedure.

The sequence of μ values used in the interior-point methods are fixed in advance as a geometrically decreasing sequence: $\mu_i = \mu_{\text{init}} \rho_\mu^{i-1}$ for $i = 1, 2, \dots, n_\mu$. The choice of parameters used is $\mu_{\text{init}} = 5 \cdot 10^{-5}$, $\rho_\mu = 0.125$, and $n_\mu = 6$. This means that the ultimate value is $\mu_{n_\mu} \approx 1.5 \cdot 10^{-9}$.

The procedure `solver` to solve one time step using the interior-point method is detailed in Fig. 3.

Note that the bulk strain-energy function $b(\mathbf{x})$ in general depends on the time step index. This is because this function $b(\cdot)$ encodes all of the boundary and loading conditions. The momentum energy term $m(\mathbf{x})$ also varies with the time step because it incorporates values of the nodal velocities from previous time steps.

The interior-point minimizer, which appears in Fig. 4, is a modification of the standard trust-region method (see, e.g., Nocedal and Wright [19]). As is standard for this method, the function m appearing in the ratio test ρ is the quadratic model, that is, $m(\mathbf{x}) := \nabla f(\boldsymbol{\xi})^T \mathbf{x} + (\mathbf{x}^T \nabla^2 f(\boldsymbol{\xi}) \mathbf{x})/2$.

The two modifications are as follows. First, instead of the usual identity matrix added to regularize the Hessian, we use the Hessian computed on an artificial preliminary problem plus a multiple of the identity. This Hessian captures the geometry of the space of $\boldsymbol{\xi}$ more accurately than a plain identity matrix and therefore leads to faster convergence. This is because the objective function $f(\boldsymbol{\xi})$ is highly anisotropic; some search directions (e.g., those that create significant interpenetration) cause a large jump in the objective, while others only a small change.

The second modification is that, in addition to the usual ratio test on function values for determining when to accept a step, the function also implements a ratio test on gradient norms, namely, the variable ρ_g appearing in Fig. 4. It follows from Taylor's theorem that the numerator of the definition of ρ_g tends to zero rapidly as $\Delta \boldsymbol{\xi}$ gets small, so a large value ρ_g indicates that the function is not behaving according to the Taylor prediction. This modification was necessary because of pathological cases of the trust region method in which the objective function decreases while the gradient blows up to infinity as the boundary of a cone is approached obliquely. Applying a ratio test to the gradient prevents such occurrences.

The routine to compute a single step of the trust-region method by finding the correct Lagrange multiplier λ appears in Fig. 5 and is standard (see [19]). The test for positive definiteness as well as the computation of the direction is carried out with sparse Cholesky factorization. The function $q(\lambda)$ appearing in this procedure is

$$q(\lambda) = \frac{1}{R} - \frac{1}{\|N^{1/2}(H + \lambda N)^{-1} \mathbf{g}\|};$$

the correct multiplier λ should satisfy either $\lambda = 0$ or $q(\lambda) = 0$, i.e., $\|N^{1/2}(H + \lambda N)^{-1} \mathbf{g}\| = R$.

8 Computation of energy balance

In this section, we describe the terms that enter into the energy balance used in two of the computational experiments of Section 9 in order to validate the method. The energy balances are computed at half-steps between the main time steps since this is where the displacements are computed by the implicit midpoint

```

FUNCTION solver( $\tau, \mathbf{u}, \mathbf{d}, H^{\text{PHASE1}}, \{H_\mu\}_\mu, \text{flag1}$ )
Determine functions  $b(\cdot), m(\cdot), b_0(\cdot), m_0(\cdot)$  for time step  $\tau$ .
 $\bar{\xi} := \bar{\xi}^*(\mathbf{u})$ 
 $M := 64; \quad \mu := \mu_1; \quad R := 1.0.$ 
/* Phase 1 to find feasible  $\mathbf{x}$  by minimizing (18).
   Variable  $M$  varies in this loop, while  $\mu$  is fixed. */
loop
  Let  $f(\cdot)$  be the objective function of (18).
   $(\mathbf{u}, \mathbf{s}_0, t, R) := \text{minimize}(f, \bar{\xi}, H^{\text{PHASE1}}, R).$ 
   $\mathbf{x} := \Pi_\tau(\mathbf{u}).$ 
  if  $(\mathbf{x}, \mathbf{s}_0)$  feasible for (14)
    break
  end if
   $M := 8M.$ 
end loop
 $\bar{\xi} := (\mathbf{x}, \mathbf{s}_0).$ 
if  $\text{flag1} == \text{PREPROCESS}$ 
   $H^{\text{PHASE1}} := \nabla^2 f(\mathbf{u}).$ 
end if
/* Phase 2 to minimize (14). Variable  $\mu$  decreases
   according to fixed schedule. */
for each  $\mu := \mu_1, \mu_2, \dots, \mu_{n_\mu}$ 
  Let  $f(\cdot)$  be the objective function of (14).
  if  $\text{flag1} == \text{PREPROCESS}$ 
    Replace  $h_\mu(\cdot)$  appearing in (14) by  $h_{\mu_1}(\cdot).$ 
  end if
   $(\xi, R) := \text{minimize}(f, \bar{\xi}, H_\mu, R).$ 
  if  $\text{flag1} == \text{PREPROCESS}$ 
     $H_\mu := \nabla^2 f(\xi)$ 
  end if
end for
if  $\text{flag1} == \text{PREPROCESS}$ 
  return  $H^{\text{PHASE1}}, \{H_\mu\}_\mu.$ 
else
  return  $R\mathbf{x} + \mathbf{u}_{\text{BC}}.$ 
end if

```

Figure 3: Solver for (12).

```

FUNCTION minimize( $f, \xi, \bar{H}, R^{\text{init}}$ )
 $\nu := \|\nabla^2 f(\xi)\|_1; \quad R := R^{\text{init}}$ .
loop
   $\Delta \xi := \text{computeDeltaXi}(\nabla^2 f(\xi), \bar{H} + 10^{-3}\nu I, \nabla f(\xi), R)$ .
   $\xi^{\text{TEST}} := \xi + \Delta \xi$ .
  if  $\xi^{\text{TEST}}$  infeasible
     $R := R/4$ .
  else
     $\rho := \frac{f(\xi) - f(\xi^{\text{TEST}})}{m(\xi) - m(\xi^{\text{TEST}})}$ .
     $\rho_g := \frac{\|\nabla f(\xi^{\text{TEST}}) - \nabla f(\xi) - \nabla^2 f(\xi)\Delta \xi\|}{\|\nabla f(\xi)\| + \|\nabla f(\xi^{\text{TEST}})\|}$ .
    if  $\rho < 1/8$  or  $\rho_g > 1$ 
       $R := R/4$ .
    else
      if  $\rho < 1/4$ 
         $R := R/2$ .
      else if  $\rho \geq 3/4$  and  $\lambda > 0$  and  $\rho_g \leq 0.125$ 
         $R := 2R$ 
      end if
       $\xi := \xi^{\text{TEST}}$ .
    end if
  end if
  if  $\lambda \leq \text{tol}_1$  and  $\|\Delta \xi\| \leq \text{tol}_2$ 
    return  $\xi, R$ 
  end if
end loop

```

Figure 4: Minimization algorithm (trust-region method)

```

FUNCTION computeDeltaXi( $H, N, \mathbf{g}, R$ )
 $\lambda_{\text{LOW}} := 0$ ;  $\lambda_{\text{HIGH}} := \infty$ ;  $\lambda := 0$ 
loop
  if  $\lambda_{\text{HIGH}} - \lambda_{\text{LOW}} < \text{tol}_3$ 
    Switch to hard-case method (see [19]).
  end if
   $G := H + \lambda N$ .
  if  $G$  is positive definite
     $\Delta \xi := -G^{-1} \mathbf{g}$ 
     $\delta := (\Delta \xi^T N \Delta \xi)^{1/2} - R$ ;
    if  $|\delta|/R < \text{tol}_4$  or ( $\delta \leq 0$  and  $\lambda \leq \text{tol}_1$ )
      return  $\Delta \xi$ 
    end if
    if  $\delta > 0$ 
       $\lambda_{\text{LOW}} := \lambda$ .
    else
       $\lambda_{\text{HIGH}} := \lambda$ .
    end if
     $\text{PosDef} := \text{true}$ ;  $\lambda := \lambda - q'(\lambda)/q(\lambda)$ .
  else
     $\lambda_{\text{LOW}} := \lambda$ .
     $\text{PosDef} := \text{false}$ .
  end if
  if  $\text{PosDef} == \text{false}$  or  $\lambda < \lambda_{\text{LOW}}$  or  $\lambda > \lambda_{\text{HIGH}}$ 
    if  $\lambda_{\text{HIGH}} == \infty$  and  $\lambda == 0$ 
       $\lambda := 1$ ;
    else if  $\lambda_{\text{HIGH}} == \infty$  and  $\lambda > 0$ 
       $\lambda := 2\lambda$ ;
    else
       $\lambda := (\lambda_{\text{LOW}} + \lambda_{\text{HIGH}})/2$ 
    end if
  end if
end loop

```

Figure 5: Subroutine of trust-region method to find one step $\Delta \xi$

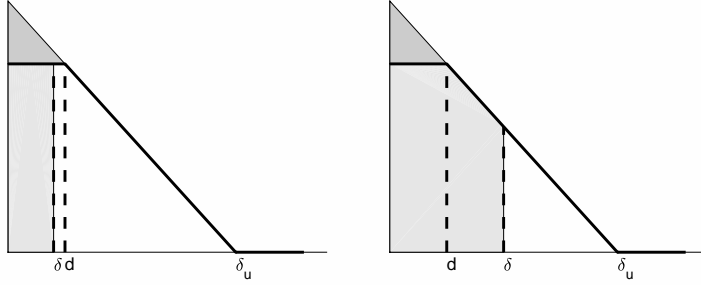


Figure 6: Plot of the computation of cohesive energy. The figure in the left considers the case $\delta < d$, where δ is the current opening displacement and d is the damage value at an interface Gauss point. The figure on the right considers $\delta > d$. Note that in a continuous-time model, one would never have $\delta > d$. In our computations, however, the update to d lags one time-step behind the computation of δ . The lightly shaded area in both figures indicates the energy that can be recovered if the interface unloads. In the plots of the next section, this is denoted as “fracture energy.” The darkly shaded area indicates dissipated energy due to irreversibility. The total cohesive energy associated with the Gauss point is therefore the sum of the two areas.

rule. We note that energy balance computations for initially rigid cohesive fracture have been used in the previous literature, e.g., by Molinari et al. [17], to derive results on convergence behavior.

Kinetic energy is evaluated using quadrature of

$$\frac{1}{2} \int_{\Omega} \rho \dot{u}^2 dV.$$

The value for \dot{u} for use in this integral is taken to be the midpoint of the velocities evaluated at two consecutive time-steps. Strain energy is evaluated using quadrature on the first term of (1) applied to the displacements at the midpoint of a time step.

For a conservative model, cohesive energy would be evaluated using quadrature on the second term of (1). However, recall that we have introduced the damage variable \mathbf{d} , so the calculation is more complicated and is described in the caption of Fig. 6.

The stored energies just described must be balanced against the work done on the models. The first source of work is from the traction and body forces (the last two terms of (1)). Since our examples do not involve either traction or body forces, we omit a detailed discussion of these terms, but their computation is relatively straightforward.

The work done by moving displacement (i.e., velocity) boundary conditions is computed as follows. The objective function $f(\mathbf{u}; \mathbf{s}_0)$ is written down as in (14), except that all functions are written in terms of \mathbf{u} (the vector of all DOFs) instead of \mathbf{x} (the vector of unconstrained DOFs). Next, the gradient with respect to \mathbf{u} is computed at the minimizer for the final value of μ . The gradient entries corresponding to the constrained DOFs will in general not vanish because the objective function is not minimized with respect to them. In fact, the gradient entries are exactly the reaction forces for those DOFs. Therefore, the work due to displacement constraints during a single time-step, that is, from one half-time-step to the next, is evaluated as follows. One computes the inner product of the time-average of these forces (average between the current half-time-step and the previous) and the distance traveled by each such DOF between the current and previous half-time-step.

Finally, work done by contact boundary conditions is also obtained as an inner product. One multiplies the contribution to the force balance from the derivative of the contact barrier term that appears in $\nabla_{\mathbf{u}} f(\mathbf{u}; \mathbf{s}_0)$ by the distance traveled. Time-averages are used as in the last paragraph. Note that although the coefficient μ in front of the barrier term may vanish, the corresponding term of the gradient does not vanish as $\mu \rightarrow 0$ but instead tends to a constant value; this is a well-known aspect of interior-point theory.

9 Computational experiments

In this section we describe three computational experiments. Experiment 1 involves impact of a metal striker on a compact compression specimen (CCS). This application demonstrates the ease in which convex constraints can be included in the computation. This problem involves three contact surfaces detailed in the next paragraph.

The CCS is made of PMMA of height \times width = 51mm \times 46mm. Its initially undeformed configuration is depicted in Fig. 7. It is initially in contact with two steel bars (left and right bar), both of which are stationary. Before contact, the striker is moving in the positive x direction at 25 m/s, and a gap exists between the striker and left bar. This computation simulates an experiment by Rittel and Maigre [26]. The striker and the left bar, the left bar and the specimen, and finally the specimen and the right bar are all contact surfaces. We model contact in each of the three surfaces via inequalities between x -coordinates of matching nodes of the two sides of the surface. Refer to Fig. 7. In our formalism, these inequalities are presented as $E\mathbf{x} \geq \mathbf{a}$ in (12). Note that prevention of interpenetration between neighboring bulk elements is modeled as a different set of linear inequalities in (12), namely, the inequalities $(s_1)_{e,\iota} \geq 0$.

No boundary conditions are applied, i.e., all boundaries are unconstrained and traction-free. The initial mesh of the CCS contains 1765 nodes and 820 element (quadratic triangles). After duplication of nodes to create interface elements, the number of nodes is $6 \cdot 820 = 4920$. The mesh near the fracture zone is an isoperimetric “pinwheel” mesh [10] transformed by a nonlinear coordinate transformation, as depicted in Figure 7. Isoperimetric meshes have the property that in the limit of mesh refinement, all possible crack orientations are represented in the mesh, so they are well suited for computations in which determining the crack path is part of the problem. (Other techniques have been proposed for representing many possible orientations in a mesh, e.g., adaptive splitting of polygonal elements by Leon et al. [15].) The three metal bars (striker, left bar, and right bar) are modeled with quadratic triangles. No interface elements are introduced in the three steel bars. The final model contains 6137 nodes and 1380 quadratic triangles.

The hyperelastic model used in the CCS is nonlinear plane stress, whose material parameters are c_1 and β (see (4)). These are obtained from the reported E and ν according to the formulas $c_1 = E/(4(1 + \nu))$, $\beta = \nu/(1 - 2\nu)$ [14]. The striker is isotropic linearly elastic.

The time step is 3 microseconds. The simulated crack path after 40 time steps (120 simulated microseconds)—refer to Fig. 8—is similar to experimental results in [26].

The test was run on a 2.6GHz Intel Xeon E5-2690 running Linux. The algorithm was coded in the Julia [3] programming language, version 1.1.0. The core computing kernel is sparse Cholesky factorization, which uses Julia’s implementation of SuiteSparse [7]. The code is not parallelized yet. The computation time for 40 time steps was 2 hours.

Property	Symbol	PMMA (Exper. 1)	Steel (Exper. 1)	Concrete (Exper. 2)	Mortar (Exper. 3)
Young modulus	E	5.76 GPa	200 GPa	38 GPa	5.98 GPa
Poisson ratio	ν	0.42	0.3	0.18	0.22
Density	ρ	1180 kg/m ³	8050 kg/m ³	—	—
Critical traction	σ_c	105 MPa	—	3 MPa	3 MPa
Mixity	β^{MIX}	2.0	—	1.5	1.0
Critical energy release rate	G_c	352 Pa·m	—	69 Pa·m	2280 Pa·m

Table 1: Material properties used in computational experiments.

We also tracked energy balance. The technique used to measure energy balance was described in Section 8. Because the optimization problem is solved at the midpoint of timesteps in the implicit midpoint rule used herein, we evaluate the energy balance at time-step midpoints. However, not all the variables are evaluated at time-step midpoints, so interpolations must be used. Therefore, we would not expect exact energy balance

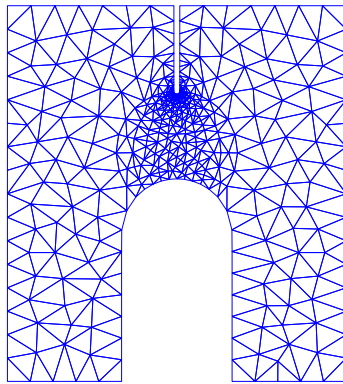
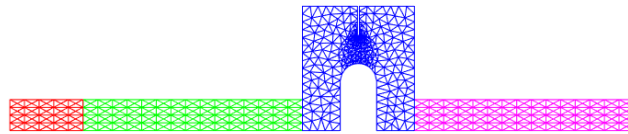


Figure 7: Initial geometry and mesh of the striker and CCS specimen (Experiment 1). The entire mesh is shown on top with each part (striker, left bar, CCS, right bar) in a different color; the initial gap between the striker and left bar is not discernable at this scale. A close-up of the CCS initial mesh appears on the bottom.

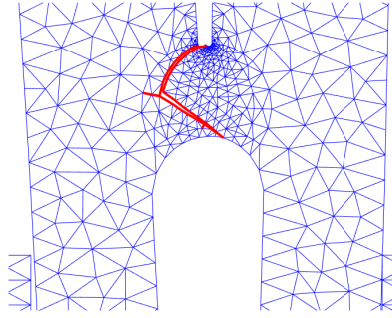


Figure 8: Damaged interfaces after 40 time steps (120 microseconds of simulated time) in Experiment 1.

because the different terms involve different approximation assumptions.

Fig. 10 compares the horizontal displacement of the left contact surface of the CCS from the computation versus an experimental measurement [25]. The comparison is imprecise because only a single number was recorded per time step by the experiment. On the other hand, the computation indicates that the left contact surface of the CCS bends inward, and therefore its horizontal displacement depends on the vertical coordinate of the measurement. To account for this, we compare the average computed horizontal displacement over the entire contact surface to the experimental measurement. Note that the time-coordinate of the experiment was shifted by hand to match the start time of the computation since the experimental data did not identify the time value when the striker collides with the left bar.

Experiment 2 exhibits the performance of the method in the quasistatic (slow loading) regime. In this problem, taken from Galvez et al. [9], a beam of concrete $15 \text{ cm} \times 67.5 \text{ cm}$, plane stress, with an initial centered slit is subjected to a moving displacement boundary condition concentrated at an off-center point. The problem set-up is described in more detail in Fig. 11.

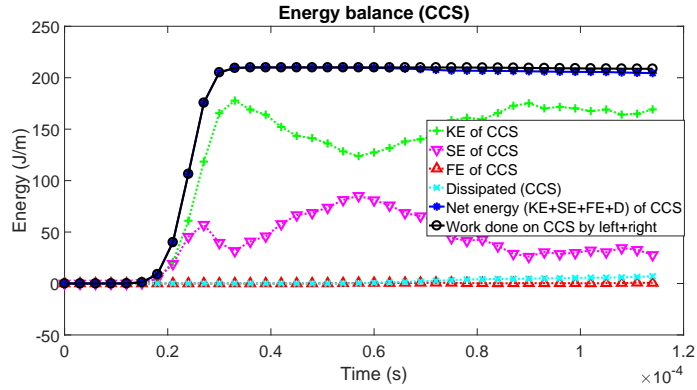
A depiction of the configuration after 26 load steps is shown in Fig. 12. The number of elements is 3168 and the number of nodes (after duplication) is 19,008. This computation required 17 hours. (The amount would be greatly reduced if we had inserted interface elements only in the zone where crack propagation is known to occur i.e., above and to the right of the initial slit, whereas in fact our mesh has cohesive interfaces at every interelement boundary.) The crack path roughly matches the experiment in [9], although we were not trying to accurately reproduce the path in this experiment because we did not use a pinwheel or other special mesh.

An energy balance was also computed for the Galvez experiment; the results are reported in Fig. 13. It is interesting to compare the energy balance in Experiment 1 versus Experiment 2. In Experiment 1, most of the work on the CCS becomes kinetic energy of the CCS. Part becomes strain energy, but the strain energy is partly released as it is transformed first to cohesive energy and then dissipated. In Experiment 2, there is no kinetic energy (the problem is quasistatic), so the energy of the load first builds up the strain energy, which is then released as cohesive energy, and then soon after the fracture energy is dissipated.

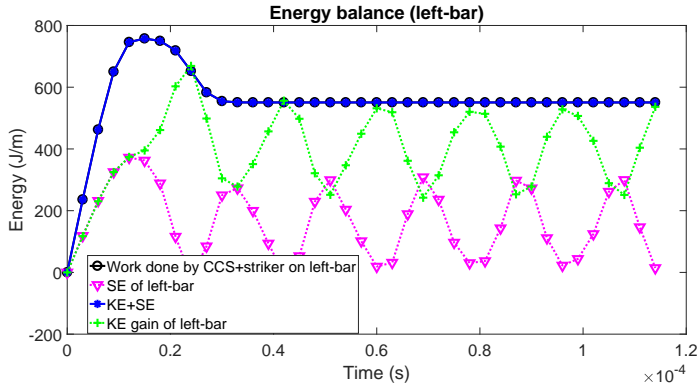
In addition, a load-displacement curve was plotted since this data is available experimentally. The result of this computation appears in Fig. 14.

Experiment 3 is also a quasistatic experiment involving a concrete mortar plate with three holes and a notch illustrated in Fig. 15. Pins that fit into the top and bottom holes pull the holes vertically apart at a rate 0.1 mm/s . This is modeled as velocity boundary conditions constraining both x - and y -coordinates of all points on the boundaries of these two holes.

Ambati et al. [1] present a computational result using their phase-field method to determine the load-displacement relationship (displacement of the top pin versus force on the top pin). Their result shows two



(a) Energy balance of CCS



(b) Energy balance of left bar

Figure 9: Energy balances for the CCS (Experiment 1); “KE” stands for kinetic energy, “SE” stands for strain energy, and “FE” stands for fracture energy. Refer to Section 8 for an explanation of how the energy and work contributions were computed. In the top figure, if energy were exactly conserved, the blue and black curves would coincide. In the bottom figure, the curves do coincide. The energy balance for the left bar indicates that it vibrates after the impact.

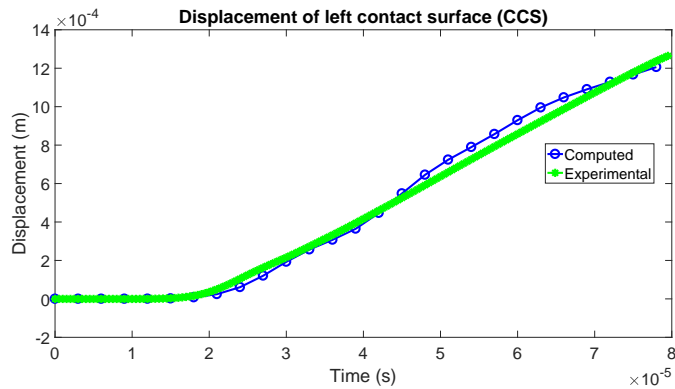


Figure 10: Comparison of experimentally measured displacement of the CCS left contact surface with the displacement computed by the method (Experiment 1). The latter is averaged over the contact surface.

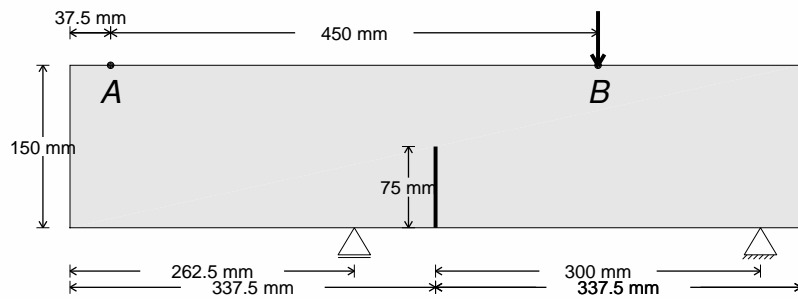


Figure 11: Experiment 2: quasistatic test of concrete beam. The beam is supported at two asymmetric points of its base and has an initial vertical slit. The point B is loaded quasistatically. The point A is referred to in Fig. 14 below.

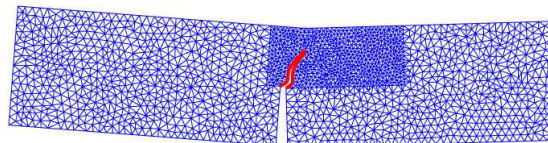


Figure 12: Final configuration of concrete beam after 25 steps. The displacements are exaggerated by a factor of 50 for better visualization.

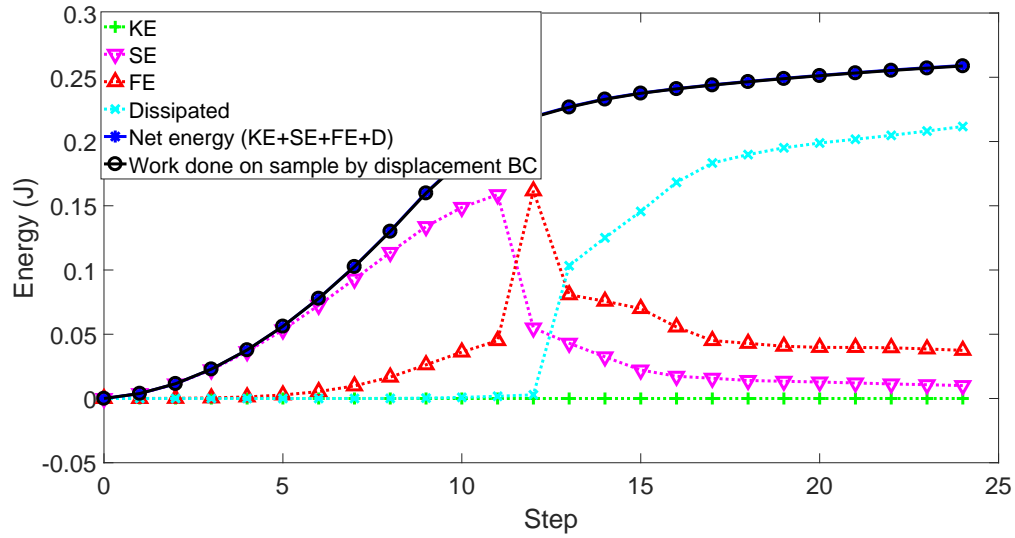


Figure 13: Energy balance for Experiment 2. Refer to the caption of Fig. 9 for further information. The last two curves are indistinguishable (coincident). Thickness has been normalized to 5cm to correspond to the experiment.

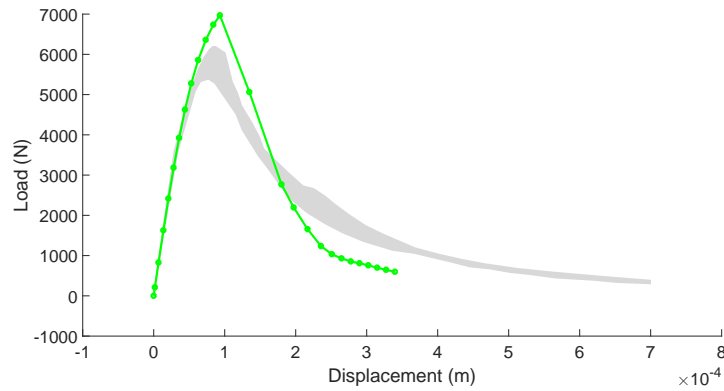


Figure 14: A plot of the load (reaction force) at point B versus the vertical deflection of point A (experiment 2). The green curve represents the data from our computation. The experimental envelope from Galvez et al. [9] is represented by gray curves. Thickness has been normalized to 5cm to correspond to the experiment.

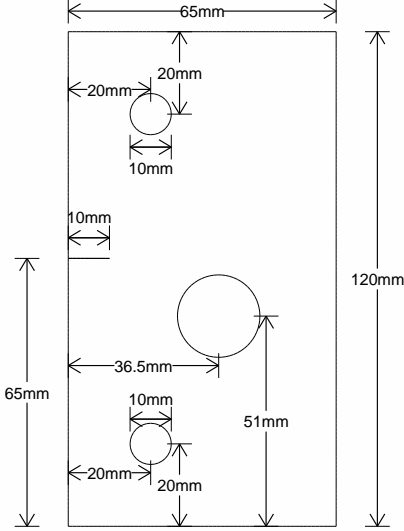


Figure 15: Experiment 3 involves a 65mm×120mm concrete plate with three holes and a 10mm-long horizontal notch on the left edge. The plate is loaded quasistatically by pins that pull the top and bottom holes vertically apart.

peaks in the load, the first at slightly more than 0.5 mm and the second at slightly less than 2 mm.

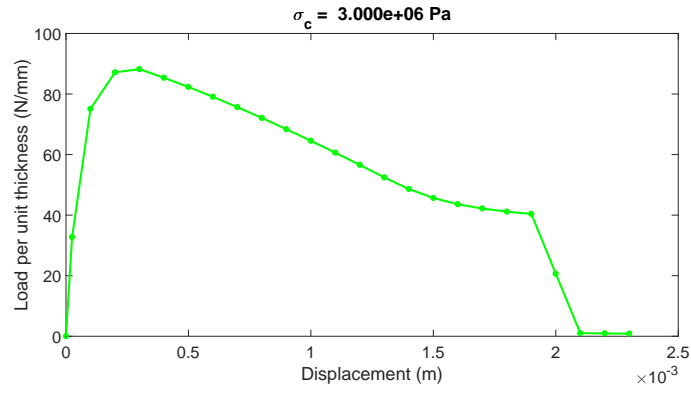
Our load-displacement plot is presented in Fig. 16. This computation required six hours per parameter choice. The load was applied at an incremental rate of 0.1 mm per step. We were unable to reproduce the second peak with the material parameters shown in Table 1. We hypothesize the following phenomenological explanation for the second peak. After the crack propagates to the large central hole, the body behaves elastically (i.e., the remaining reverse C-shaped piece flexes elastically) until a second crack starts on the right of the big hole. Our computational experiment, however, shows that the second crack on the right of the big hole is mostly formed by time the first crack reaches the big hole, so no elastic behavior is observed after the first crack reaches the big hole.

The phenomenological explanation in the previous paragraph suggests that our method could obtain the second peak if we increase σ_c , thus delaying the nucleation of the second crack. We tested this hypothesis by raising σ_c by a factor of 20 (to $6.0 \cdot 10^7$ Pa) and by a factor of 40 (to $1.2 \cdot 10^8$ Pa). Note that these numbers are significantly higher than the usual reported critical stress for concrete mortar. With these modified values of σ_c we indeed observed a second peak as in Fig. 16, but even at $\sigma_c = 1.2 \cdot 10^8$ the displacement at the position of the second peak falls well short of 2mm.

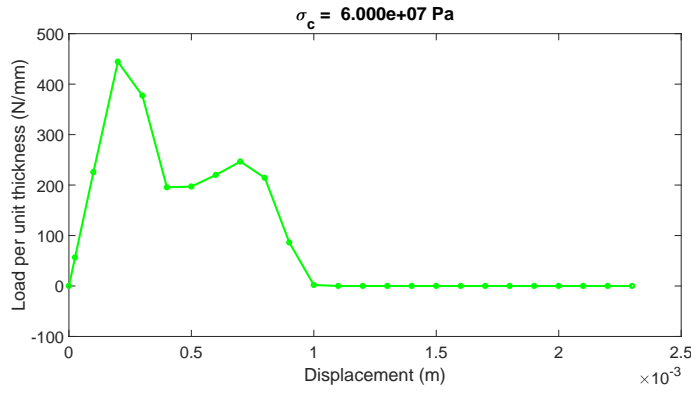
The phase-field method used in the Ambati computation does not have σ_c as a material parameter. The discussion in the previous paragraph raises the question of what value of σ_c corresponds to the Ambati computation. Some authors (see, e.g., eq. (27) of Borden et al. [4]) have proposed that the length-regularization parameter in phase-field models is linked to σ_c . Experiment 3 may provide an example for future investigation of the connection between length-regularization in such phase-field methods and σ_c in cohesive models. A phase-field regularized cohesive model that involves σ_c as a material parameter and frees previous implementations of phase-field method from the above limitation has been recently proposed in Geelen et al. [11].

The crack-paths for all three values of σ_c are shown Fig. 17 as well as the laboratory experimental path. The first part of the crack path is sensitive to σ_c but the second part is not.

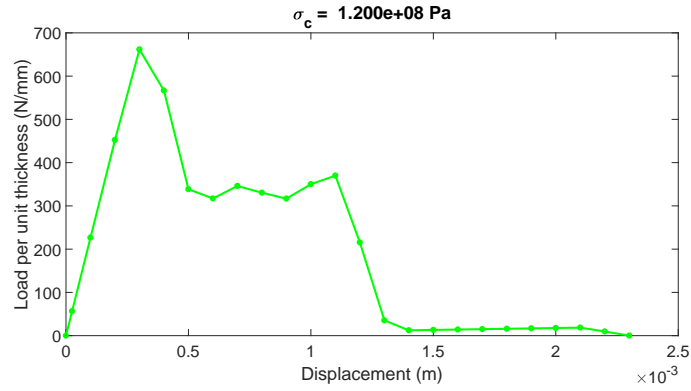
A fourth computational experiment not reported here was a branching dynamic crack model used frequently in the literature (see, e.g., Borden et al. [4]) in which a rectangular specimen with a horizontal notch is subject to vertical traction loading. This traction load causes a horizontal crack to propagate from the



(a)



(b)



(c)

Figure 16: Load-displacement curve for Experiment 3 with three different values of the material parameter σ_c . Higher values of σ_c are able to reproduce the double peaks reported in Ambati et al. [1].

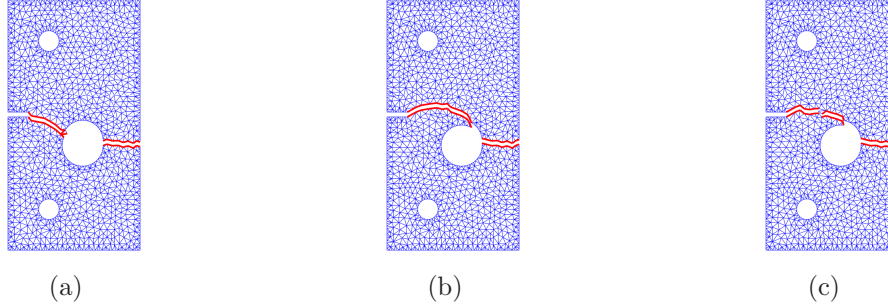


Figure 17: Crack-path in Experiment 3 for three different values of σ_c .

notch. After a small distance of horizontal propagation, the crack branches, yielding a crack with a tilted “Y” shape. We found that our method produced a branch with the correct shape, but the straight part of the crack was too long compared to other computations in the literature. We subsequently observed that the branch started at the correct position when the method was re-run with a very small time step, requiring a simulation that ran for nearly a week. This is a limitation not of our method specifically but rather of all methods based on implicit time-step rules. In problems in which the time step must be small enough to capture highly dynamic and unstable behavior, implicit time-stepping is generally not recommended. Refer to the recent paper [12] by the second and third authors for an explicit time-stepping method that uses energy principles similar to those herein.

10 Summary and conclusions

An interior-point method for initially rigid cohesive fracture is proposed. A key technical step to make this method possible is the replacement of an equation relating the effective opening displacement to the coordinate entries of the opening displacement by an inequality constraint.

The specific optimization models introduced herein are as follows.

- Model (11) is the fundamental optimization problem that introduces all the energy terms into the objective and the constraints relating the bulk-node displacements \boldsymbol{x} to opening displacements \boldsymbol{s}_0 .
- Model (12) is identical to (11) except for replacing an equality constraint with an inequality constraint that yields a mathematically equivalent optimization problem (i.e., same optimizers). This replacement makes the model amenable to an interior-point method.
- Model (13) replaces the conic inequality constraints in (12) with self-concordant barrier functions in the objective as is the usual practice in the development of an interior-point method. As the barrier parameter $\mu > 0$ tends to 0, a solution to (12) is recovered from the solution to (13).
- Model (14) is mathematically equivalent to (13); the modification is that substitution has been used to eliminate the equality constraints. The main work of the code is the solution of (14).
- Model (17) is the artificial problem solved in Phase I to obtain an initial feasible solution to (14). This model introduces the artificial variable t .
- Model (18) further develops (17) to obtain an initial feasible solution in which all elements are non-inverted even in the presence of moving displacement boundary conditions. This is accomplished by changing variables from \boldsymbol{x} (unconstrained boundary DOFs) to \boldsymbol{u} (all boundary DOFs). The boundary conditions are represented by equality constraints on \boldsymbol{u} , but (18) enforces these equality constraints as inequalities involving the artificial variable t to ensure that a feasible starting point exists for a known solution \boldsymbol{u} with no inverted elements.

A summary of the computational procedures presented is as follows.

- The top-level procedure appears in Fig. 2. Its loop is over time-steps or load steps. It also maintains and updates the damage variables. In addition, on every third step it recomputes the matrices used in regularizing the trust-region method.
- The two main loops of the interior-point method appear in Fig. 3. The first loop is Phase I in which (17) is solved in order to obtain a feasible starting point for (14). The second loop is Phase II in which (14) is solved for a decreasing sequence of μ 's.
- The solver for a specific instance of either (17) or (14) (i.e., for one particular value of M or μ) is a trust-region method, which is detailed in Fig. 4 and Fig. 5. The trust-region method is necessary due to the nonconvexity of the energy functional; it replaces the Newton loop that would be present in a conventional convex interior point method.

Computational tests show that the method is practical for quasistatic and moderately fast dynamic problems and can easily encompass additional conic inequality constraints.

11 Acknowledgements

The authors thank M. Ambati for helpful discussion regarding Experiment 3. The authors thank the referees for their careful reading and valuable suggestions for revising the paper.

References

- [1] Marreddy Ambati, Tymofiy Gerasimov, and Laura De Lorenzis. A review on phase-field models of brittle fracture and a new fast hybrid formulation. *Computational Mechanics*, 55(2):383–405, Feb 2015.
- [2] G. I. Barenblatt. The mathematical theory of equilibrium cracks in brittle fracture. *Advances in Applied Mechanics*, 7:55–129, 1962.
- [3] J. Bezanson, A. Edelman, S. Karpinski, and V.B. Shah. Julia: A fresh approach to numerical computing. *SIAM Rev.*, 59(1):65–98, 2017.
- [4] M. J. Borden, C. V. Verhoosel, M. A. Scott, T. J. R. Hughes, and C. M. Landis. A phase-field description of dynamic brittle fracture. *Comput. Methods Appl. Mech. Engrg*, 217-220:77–95, 2012.
- [5] B. Bourdin, G.A. Francfort, and J.-J. Marigo. The variational approach to fracture. *J Elasticity*, 91(1-3):5–148, 2008.
- [6] Miguel Charlotte, Jérôme Laverne, and Jean-Jacques Marigo. Initiation of cracks with cohesive force models: a variational approach. *European J. Mechanics - A/Solids*, 25:649–669, 2006.
- [7] Timothy A. Davis. *Direct methods for sparse linear systems*. SIAM, Philadelphia, 2006.
- [8] D. S. Dugdale. Yielding of steel sheets containing cracks. *J. Mech. Phys. Solids*, 8:100–104, 1960.
- [9] J.C. Gálvez, M. Elices, G. V. Guinea, and J. Planas. Mixed mode fracture of concrete under proportional and nonproportional loading. *International J. Fract.*, 94(3):267–284, 1998.
- [10] P. Ganguly, S. A. Vavasis, and K. D. Papoulia. An algorithm for two-dimensional mesh generation based on the pinwheel tiling. *SIAM J. Scientific Computing*, 28(4):1533–1562, 2006.
- [11] Rudy J. M. Geelen, Yingjie Liu, John E. Dolbow, and Antonio Rodríguez-Ferran. An optimization-based phase-field method for continuous-discontinuous crack propagation. *International Journal for Numerical Methods in Engineering*, 116(1):1–20, 2018.

- [12] M. R. Hirmand and K. Papoulia. Block coordinate descent energy minimization for dynamic cohesive fracture. *Comput. Methods Appl. Mech. Engrg*, 354:663–688, 2019. <https://doi.org/10.1016/j.cma.2019.05.051>.
- [13] M. Reza Hirmand and Katerina D. Papoulia. A continuation method for rigid-cohesive fracture in a discontinuous Galerkin finite element setting. *International Journal for Numerical Methods in Engineering*, 115(5):627–650, 2018.
- [14] J. K. Knowles and E. Sternberg. Large deformations near a tip of an interface-crack between two Neo-Hookean sheets. *J. Elasticity*, 13:257–293, 1983.
- [15] S. E. Leon, D. W. Spring, and G. H. Paulino. Reduction in mesh bias for dynamic fracture using adaptive splitting of polygonal finite elements. *Int. J. Numer. Meth. Engrg*, 100:555–576, 2014.
- [16] E. Lorentz. A mixed interface finite element for cohesive zone models. *Comput. Methods Appl. Mech. Engrg*, 198:302317, 2008.
- [17] J. F. Molinari, G. Gazonas, R. Raghupathy, A. Rusinek, and F. Zhou. The cohesive element approach to dynamic fragmentation: The question of energy convergence. *Int. J. Numer. Meth. Engrg*, 69:484–503, 2007.
- [18] Yurii Nesterov and Arkadii Nemirovskii. *Interior-Point Polynomial Algorithms in Convex Programming*. SIAM, 1994.
- [19] J. Nocedal and S. Wright. *Numerical Optimization, 2nd Edition*. Springer, New York, 2006.
- [20] M. Ortiz and A. Pandolfi. Finite-deformation irreversible cohesive elements for three dimensional crack propagation analysis. *Int. J. Numer. Methods Eng.*, 44:1267–1282, 1999.
- [21] K. D. Papoulia. Non-differentiable energy minimization for cohesive fracture. *Int. J. Fracture*, 204:143–158, 2017.
- [22] K. D. Papoulia, C.-H. Sam, and S. A. Vavasis. Time continuity in cohesive finite element modeling. *Int. J. Numer. Methods Eng.*, 58(5):679–701, 2003.
- [23] R. Radovitzky, A. Seagraves, M. Tupek, and L. Noels. A scalable 3d fracture and fragmentation algorithm based on a hybrid, discontinuous Galerkin, cohesive element method. *Computer Methods in Applied Mechanics and Engineering*, 200(1-4):326–344, 2011.
- [24] J. R. Rice. The localization of plastic deformation in theoretical and applied mechanics. pages 207–220. North-Holland, 1976.
- [25] D. Rittel. Private communication, 2018.
- [26] D. Rittel and H. Maigre. A study of mixed-mode dynamic crack initiation in PMMA. *Mechanics Research Communications*, 23(5):475–481, 1996.
- [27] M. J. Todd. A study of search directions in primal-dual interior-point methods for semidefinite programming. Available from <http://ecommons.cornell.edu>, 1999.
- [28] Y. Wang and H. Waisman. From diffuse damage to sharp cohesive cracks: A coupled XFEM framework for failure analysis of quasi-brittle materials. *Computer Methods in Applied Mechanics and Engineering*, 299:57–89, 2016.
- [29] H. Yamashita and H. Yabe. A primal-dual interior-point method for nonlinear optimization over second-order cones. *Optimization Methods and Software*, 24:407–426, 2009.
- [30] Y. Ye. *Interior Point Algorithms: Theory and Analysis*. Wiley, 1997.